A multi-scale strategy to predict fretting-fatigue endurance of overhead conductors

J. Said, S. Garcin, S. Fouvry, Georges Cailletaud, C. Yang, F. Hafid

A multi-scale strategy to predict fretting-fatigue endurance of overhead conductors

J. Said[1,2,3], S. Garcin[1], S. Fouvry[1], G. Cailletaud[2], C. Yang[3], F. Hafid[3]

[1] Ecole Centrale de Lyon, UDL Univ. de Lyon, LTDS-CNRS 5513, 36 Avenue Guy de Collongue, 69134 Ecully, France

[2] MINES ParisTech, PSL Research University, MAT-Centre des Matériaux, CNRS UMR 7633, BP87, 91003, Evry, France

[3] RTE - Direction de la R&D - Pôle Smartlab, 92073 PARIS LA DEFENSE CEDEX

(corresponding authors : Julien.said@ec-lyon.fr; Siegfried.fouvry@ec-lyon.fr)

Abstract : Overhead conductors enduring aeolian vibrations are subjected to fretting fatigue damage. To predict the fretting fatigue cracking risk along the conductor-clamp assembly involving a multitude of crossed-strands contacts, a multi-scale analysis is considered. First, a global model provides the spatial distribution of normal, tangential and fatigue loadings for every contact. "Specific" loading cases were simulated using a local FEM model involving a Crossland fatigue stress analysis and a critical distance approach to correct the stress-gradient effects. Mono-contact fretting fatigue experiments were then performed reproducing the exact same loading cases. The comparison between numerical predictions and experimental results showed that a very good prediction of crack-nucleation is achieved using this strategy. However, total failures were not systematically observed. It is believed to be related to the manufacturing process. Wire drawing induces a longitudinal microstructure which promotes cracks with a low diving angle, rather than cracks propagating directly into the bulk. 3D-surface-crack simulations confirm a crack arrest phenomenon induced by the contact-induced compressive stress field.

Keywords: Fretting Fatigue; overhead conductors; Crack Nucleation; Global-Local FEA simulations

1. Introduction

Wire rope assemblies are widely used in civil engineering in structures such as cable supported bridges, cranes, elevators and ski lifts, but also in transmission power lines. These cable structures offer a very good compromise between tensile strength and bending capabilities, given their small size. In the case of transmission lines, even if their primary purpose is to conduct electricity, their mechanical behavior remains a key point for any transmission system operators (TSO) as mechanical failures may ultimately affect the energy transportation.

The overhead conductors in these lines are, just like every other wire rope, composed of multilayered helical strands (figure 1b) that can be made of quasi-pure aluminum, steel or aluminum alloys. All these strands are subjected to a large number of contacts with their neighbors, within the same layer or between adjacent ones [1]. At these contacts, any kind of external solicitations, such as wind induced vibrations may result in small oscillatory movements under pressure (figure 1c). This kind of tribological loading is known as fretting, and is believed to be responsible of a lot of strand failures observed on aged conductors. As a matter of fact, the alternated bending of the conductor generates fatigue loadings that can propagate cracks nucleated due to fretting mechanisms, resulting in so-called fretting-fatigue processes.

Fretting induced strand failures on conductors have already been reported in 1968 by Fricke [2] and during the following decades, several authors have studied this phenomenon applied to transmission lines. Many studies have been using dedicated test benches for a whole cable or a single strand [2-6] while other focus on observations realized on already used and aged conductors [6]. Moreover, as the clamping zone has been pointed out as the critical area where the majority of failures occur [7-8], most of the recent benches include a clamp combined with bending loadings to get closer to reality. Zhou [9-11] also proposed a damage mapping of the outer layer of a conductor focused on this clamping zone, shedding more light to this particular area.

Fewer studies have been carried out using numerical modeling and Finite Element Analyses (FEA) and especially on conductors, as most of them concern steel cables and wear modeling between thin steel strands. On this specific topic, Cruzado [12 – 14] first studied wear for such a configuration before addressing the wear-cracking competition. Wang [15] also used a local model focused on a single contact to assess the crack nucleation risk in fretting-fatigue for hoisting cables. In addition to this local model, the same author presented in another study a macroscopic model simulating the whole steel cable and its mechanical behavior. But, as it has a very complex structure inducing a very high computational cost, it can only model a short portion of the cable. To avoid these computational limitations, Lalonde [16-18] proposed a numerical modeling of a conductor using beam elements instead of volume elements commonly used in 3D FEA. This approach allows representing a very long portion of a conductor and its interaction with a clamp for a very low numerical cost thanks to the light mesh used. While it is very suitable for fatigue modeling of a conductor, it may be a bit more limited for more accurate tribological characterizations of the interactions between strands

The method proposed in the present work consists in a FEM modeling of a clamped conductor at two distinct scales, coupled with experimental tests to support these numerical models. The first one is a "global" model representing a whole conductor and a simplified clamp, and the other one is a "local" model that focuses on a single contact between two individual strands. With its macroscopic scale, the global model can assess the distribution of contact forces along the axis of the studied conductor, and these data can then be used as input for the local model to estimate the cracking risk. A key issue to predict fretting fatigue cracking is the very severe stress gradients imposed by the contact loading. Hence non-local fatigue stress analyses like process volume stress averaging [19] or critical distance method [20] need to be considered. Thus, to calibrate the chosen critical distance method, plain fatigue and plain fretting tests have been performed and post processed to establish the plain fatigue limits associated with the representative critical distance length scale. Using these fatigue limits and this length scale the analysis will consist in predicting the fretting fatigue limit. The predictions concerning the strand failure are based on the hypothesis that any cracked strand is considered broken (i.e. the

crack propagation is neglected). This hypothesis may also be discussed according to the results obtained through this study concerning the propagation behavior.

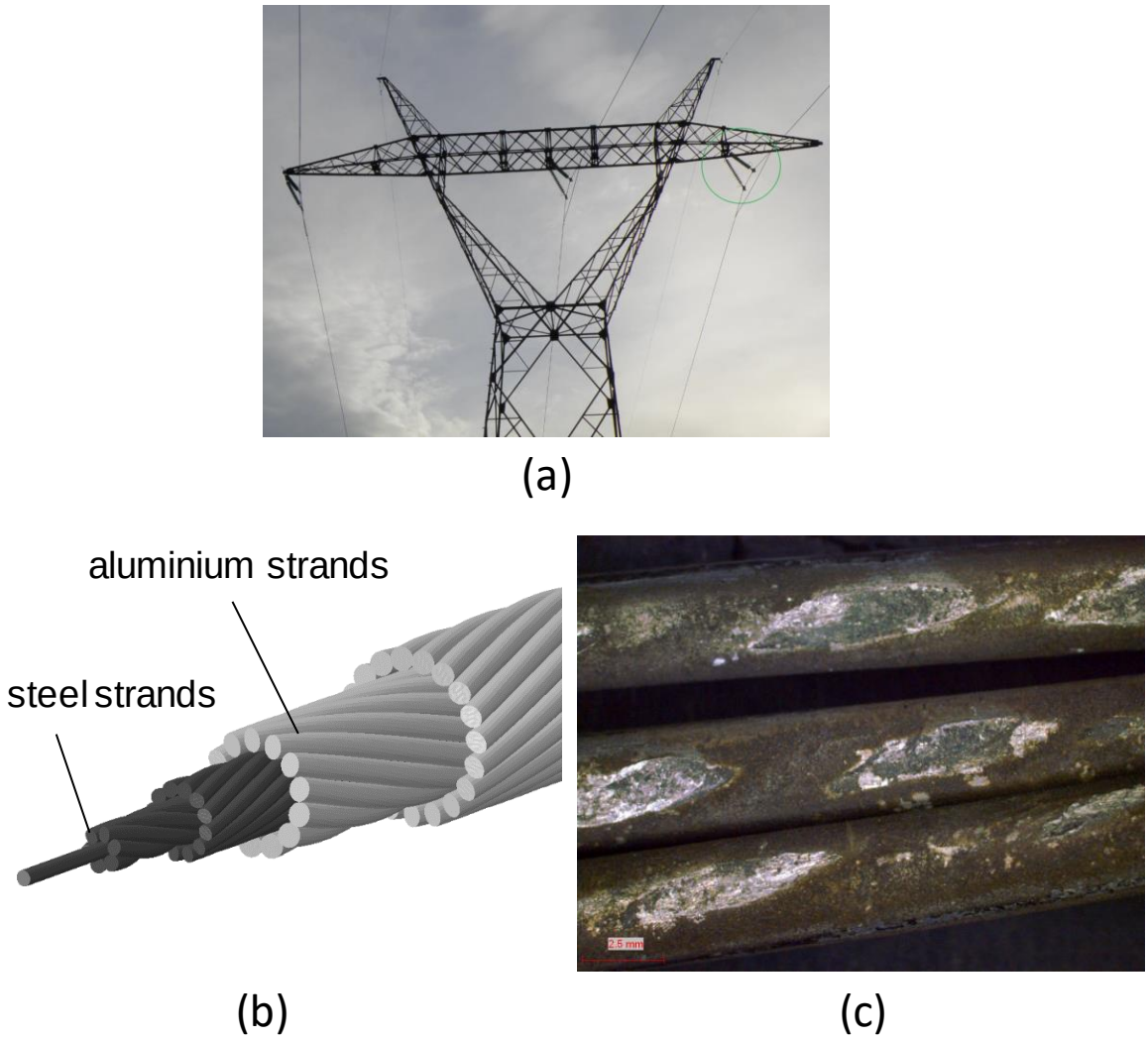

Figure 1: (a) Electric pylon exploited by the french TSO ; (b) Rendering of the studied ACSR, with aluminum strands in light grey ; (c) Potential fretting scars observed on the aluminum outer layer of an aged conductor, extracted from the clamping zone

2. Materials and experimental testing

2.1. Conductor and materials

Among all the existing designs of overhead conductors, this study focuses on the behavior of an Aluminum Conductor Steel-Reinforced (ACSR) represented in figure 1b. The two outer layers are

made of quasi-pure aluminum (purity > 99%), essentially used for its conductive properties. They have for each strand a diameter of 3.60 mm and are represented in light grey on figure 1b. The inner layers, in dark grey on the same figure, are made of steel and are used to ensure the mechanical strength of the structure, with a diameter of 2.40 mm. However, a very low number of breaks among these steel strands were observed by the French TSO, so it has been decided to investigate the aluminum layers only, and more specifically the contacts between the outer layer and its neighbor. As the strands from these two layers have distinct lay angles, the relative angle for two contacting strands is quite constant and equal to 30°. This geometrical value will be retained for all further numerical and experimental setups to replicate this contact.

2.2. Plain Fatigue tests

As presented in section 3.2.2, the use of the chosen multiaxial fatigue criterion requires to know two fatigue properties of the material: the alternate fatigue limit σ_d and the torsion fatigue limit τ_d. Thus, plain fatigue tests were performed to assess these data. Raw straight strands were not available, so all the samples used were extracted from a spool sent by a conductor manufacturer. These strands went through all the usual manufacturing processes, and were manually reshaped into straight samples.

Another consequence of the strand geometry is related to the location of the fatigue breaks. A sample has a simple and thin cylinder shape, thus most of the breaks happen at the jaws of the bench. To avoid that, the samples were systematically machined using Silicon Carbide (SiC) grinding papers to create a thinner area away from the jaws. The papers were used with a special attention being given to the surface roughness of the new surface created. Finally, the new minimum diameter was measured to calculate the new tensile stresses that would lead to failure. As the initial diameter of a strand is 3.6 mm, the new diameter after machining was systematically between 2.8 and 2.6 mm (figure 2a). The resulting effective distance was also suitable with tensile/compressive tests without any buckling. This surface finishing may affect the strand fatigue response, as it removes surface material with residual stress induced by the manufacturing process. However, it stands as the best compromise found to

avoid failures at the jaws. This choice was also justified by the fact that σ_d and τ_d are usually bulk material properties. Still, this underlines the importance of further experimental calibrations as described in section 3.2.3. to ensure the validity of the proposed strategy.

Moreover, these samples were not suitable for plain shear fatigue tests: even with the shortest samples and the rather low torque applied (< 0.5 Nm), the resulting rotational strain would not respect the infinitesimal strain hypothesis.

Figure 2b shows a typical S-N curve corresponding to a positive loading ratio. According to these tests, the fatigue limit at R = 0.2, 10^7 cycles, was established at $\sigma_{max,0.2,10^7} = \mathbf{120\ MPa}$. Similar tests conducted at R = 0.1 gave $\sigma_{max,0.1,10^7} = 115\ MPa$ and for alternated loadings (i.e. R = -1), the tensile/compressive fatigue limit $\sigma_{max,0.1,10^7} = \sigma_d = 65\ MPa$. The fatigue data are compiled in table 1.

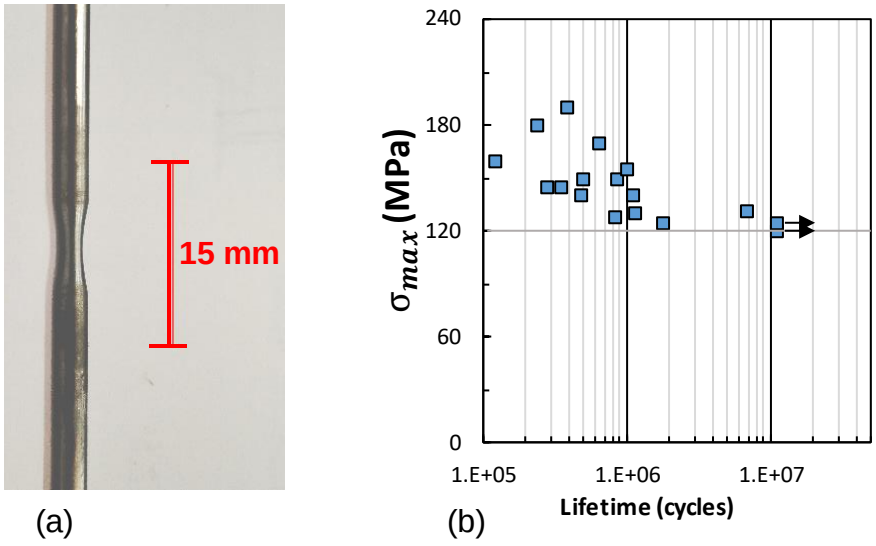

Figure 2: (a) machined sample suitable for plain fatigue tests; (b) S-N curve for the loading ratio R = 0.2 of the aluminium strands tested in this study

2.3. Plain fretting tests

To assess the tribological behavior of a single contact configuration (figure 3a) and study the crack nucleation threshold, plain fretting tests were performed. The lower sample is fixed while the other one is moved using an electromagnetic shaker with a constant frequency at 20 Hz. As represented in figure 3a, a normal force P is applied using dead weights on the contact and, when the upper sample is moved by a displacement amplitude $\delta(t)$, a tangential force $Q(t)$ is induced. The tangential force Q is measured by a piezoelectric sensor, while a LASER sensor is used for δ allowing to plot the $Q - \delta$ fretting cycle, from which are extracted Q^* and δ^* the tangential force and displacement amplitudes, respectively.

These tests were conducted in order to investigate two aspects. The first one is the determination of the sliding transition coefficient μ_t which corresponds to the transition between partial and gross slip. This tribological data is assessed using variable displacement tests as described by Voisin et al. [21]: for a constant normal load P, the tangential force amplitude Q^* is monitored as a function of the displacement amplitude δ^*, progressively increasing. For each value of δ^*, 5000 cycles are applied so the contact can stabilize. While the contact remains in partial slip, Q^* linearly increases with the displacement δ^*, until it reaches a maximum value Q_t associated with $\mu_t = Q_t/P$ at the sliding transition. After this limit point, as the applied displacement keeps increasing, Q^* collapses before stabilizing and the contact switches to gross slip regime (G.S). This decrease is due to the fact that when the contact shifts to gross slip, a debris layer is formed and the Coefficient of Friction (COF) is reduced. Such a test is illustrated figure 4b with the evolution of μ plotted versus the applied displacement. Similar tests were carried out for various normal loadings to check that the transition μ_t is not influenced by this parameter (figure 4b).

The other investigated aspect concerns plain fretting cracking under partial slip conditions (i.e. without surface wear interferences). Keeping constant the normal force at P = 300 N, the analysis consists in imposing a constant Q^* partial slip tangential force amplitude for a fixed a number of cycles before appraising the projected crack length “b” using cross section observations (fig 5). A first series of tests

was conducted for 3.10^5 cycles. Then, a few more tests were done with the same parameters but for 10^6 cycles to ensure that cracks have already reached their crack arrest final length. And as shown in figure 6, for both lifetimes cracks display similar depths.

Figure 6 plots the evolution of the measured crack depth b as a function of the applied tangential force amplitude Q^*. It appears that for $Q^* < 75$ N, cracks are whether nonexistent or rather short, and there is no visible tendency in the crack depth evolution. Then, for $Q^* > 75$ N, a sharp increase of crack depth is observed starting at b = 50 µm. From these data, the crack nucleation threshold is thus identified at $Q_{CN} = 75$ N and corresponds to the crack nucleation length $b_{CN} = b(Q_{CN}) = 50$ µm. This tangential force threshold combined with the obtained fatigue limits will be considered in the following section to identify an optimized critical distance related to the studied stress gradient conditions.

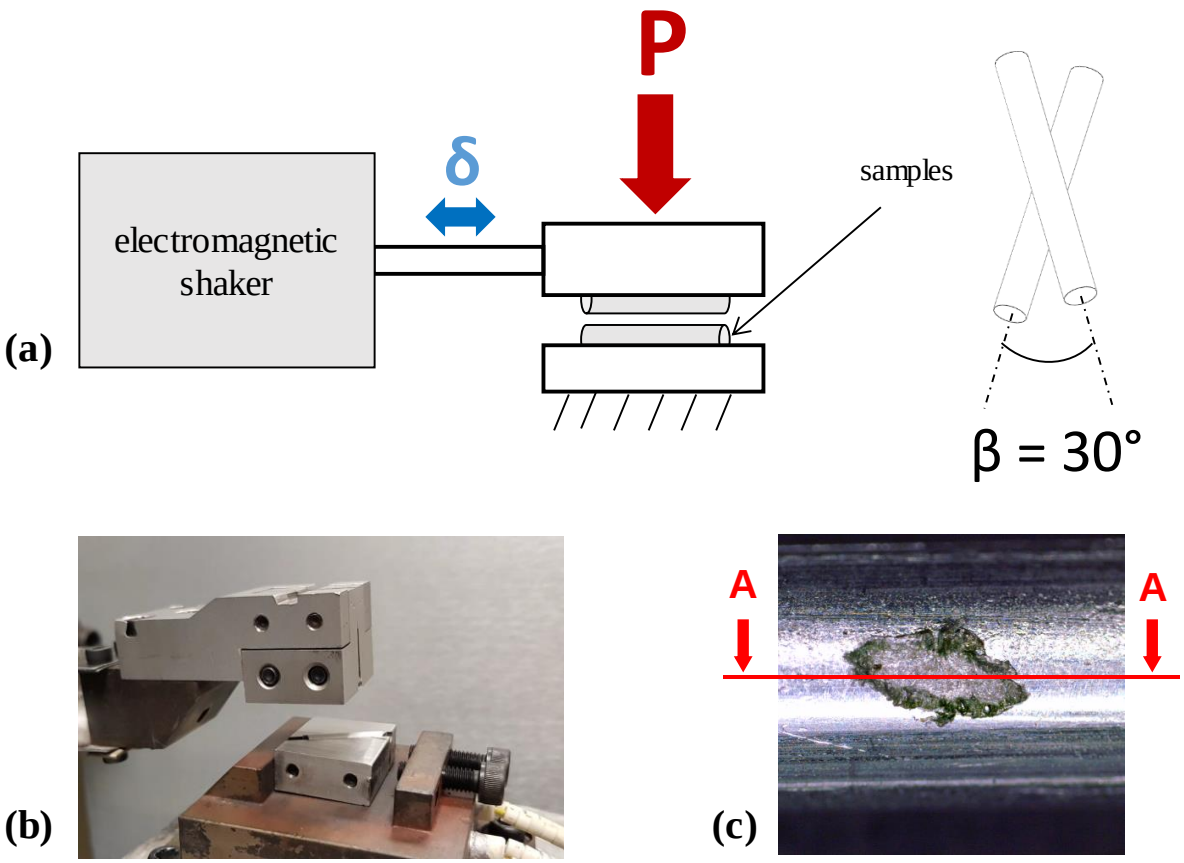

Figure 3: (a) Schematic drawing of the plain fretting test bench used ; (b) picture of the sample holders of the corresponding bench; (c) elliptical fretting scar induced by partial slip conditions displayed with a typical cutting plane used for crack length measurements ($Q^* = 100$N, P = 150N, $N=3.10^5$ cycles)

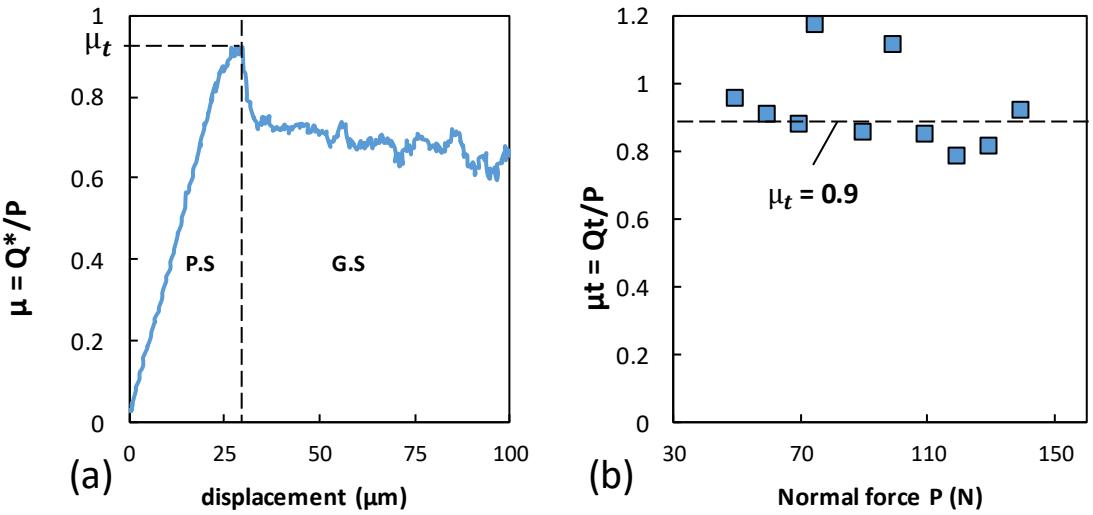

Figure 4 (a): Evolution of the Q*/P ratio during a variable displacement test (P = 140N); (b): the partial-to-gross slip transition coefficient μ_t for various normal loads

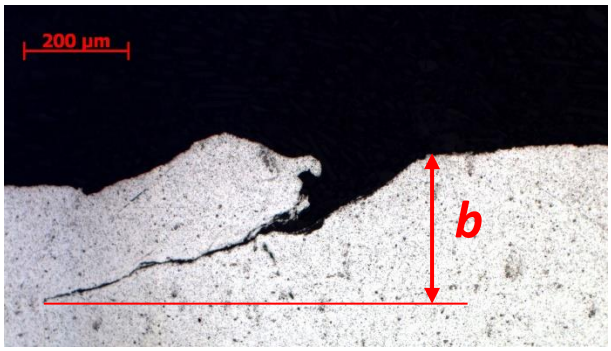

Figure 5 : Cross-section view of the plane A – A (figure 3c) and measurement of the projected crack length (Q* = 200N, P=300N, N=300k cycles)

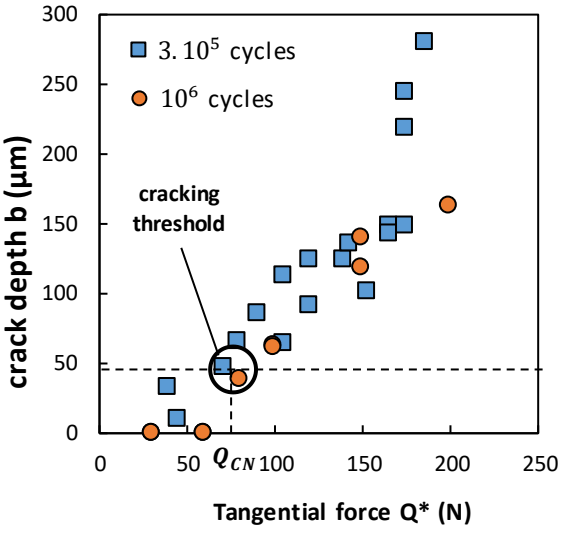

Figure 6 : Crack length versus the tangential force applied for plain fretting tests in partial slip, showing the determination of the plain fretting cracking threshold. The normal load was kept constant at P = 300 N

3. Modeling strategy and Finite Element Analysis (FEA)

3.1. FEM Simulation of the fretting crack nucleation threshold

A relevant prediction of fretting fatigue cracking risk requires to take into account the stress gradient effects [20]. One strategy consists in computing a multiaxial fatigue criterion. However, rather than considering the hot spot stress, this criterion needs to consider an averaged stress path. Such a non-local fatigue stress analysis of a fretting cracking was first developed using a process value stress analysis (i.e. the stress state used to compute the crack nucleation risk is previously averaged over a representative material volume [19]). A simpler strategy consists in considering a local stress state but at a critical distance l_{opt} below the surface hot spot stress [22]. A key issue is the definition of the relevant value of the length scale parameter l_{opt}. Taylor *et al* suggested that it must be related to the half value of the crack length transition from short to long crack propagation regime ($l_{opt} = b_0/2$). Such an approach allows a prior estimation of the critical distance to be made using conventional fatigue properties of the studied material. However, it does not consider the stress gradient level of the studied interface, which can display significant fluctuations depending on the contact size [23]. Then, the critical distance method [24] consists in identifying the optimal critical distance from a post processing analysis of plain fretting or fretting fatigue experiments defining the crack nucleation condition. This strategy was successfully adapted for many contact configurations like cylinder/plane or punch/plane contacts. More recently this post-processing calibration of the optimal distance was derived to consider finite fretting fatigue endurances by Gandiolle [24-26] and co-authors.

We currently adopted the latter approach. The optimal distance was calibrated based on plain fretting tests. Then, this value was transposed and applied for fretting fatigue tests. The corresponding results are presented in section 3.3.3.

3.2. FEM Simulation of the crossed strand plain fretting experiment

3.2.1. Single-contact modeling

The contact between two aluminium strands is reproduced using two half cylinders in contact with a relative angle of 30° as represented in figure 7. Each strand has a diameter of 3.6 mm and hexahedral volume elements were used with a refined mesh in the contact zone. The friction behavior was modeled using the Lagrange multiplier friction formulation available with the ABAQUS/Standard solver, with an associated coefficient of friction set at $f = 0.9$.

For all tested cases, the fatigue bulk stress noted $\sigma_f(t)$ is applied on the lower half-cylinder while the upper one creates the fretting loading. All of the boundaries conditions described below are applied through reference points (RF) defined in the ABAQUS/cae interface. Each simulation includes three steps:

- A displacement indentation step where a very low displacement is applied on the upper part to initiate the contact with its counter-body
- A force indentation step where the proper normal load P is applied
- A fretting cycle step where the tangential load is applied using a sine wave amplitude. At the end of this step, a complete cycle is achieved

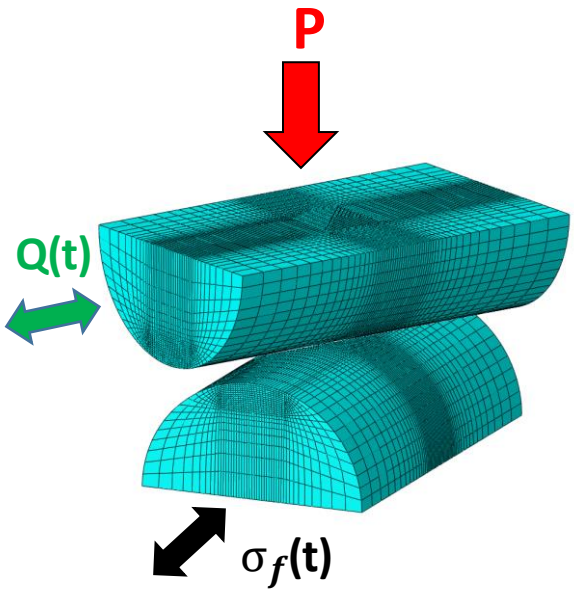

Figure 7. Mesh grid used for the local model representing a single contact between two aluminium half-cylinders. For plain fretting simulations, $\sigma_f(t)=0$.

For this first approach, the model only considers an isotropic and purely elastic material, with a Young's modulus E of 65 GPa and a Poisson ratio ν of 0.34 which were experimentally identified. However, as aluminum is a rather soft material, it may be relevant to take into account plasticity effects or anisotropic characteristics induced by the manufacturing process. This would be one of the main topic for further investigations regarding local modeling of the inter-strand contact.

3.2.2. Post-processing and Crossland criterion

The objective of the local model is to estimate the crack nucleation risk using a multiaxial fatigue criterion. The criterion used for this study is the one proposed by Crossland which depends on the tension/compression fatigue limit σ_d as well as the torsion fatigue limit τ_d. It is expressed as follows:

$$\sigma_c = \sqrt{J_{2,a}} + \alpha_C . \sigma_{H,max} > \tau_d \quad (3)$$

$$\alpha_C = \frac{\tau_d - \sigma_d/\sqrt{3}}{\sigma_d/\sqrt{3}} \quad (4)$$

In these expressions, $J_{2,a}$ represents the the second invariant of the deviatoric stress amplitude tensor during a loading cycle, while $\sigma_{H,max}$ is the maximum value of the hydrostatic pressure σ_H during a cycle. According to this criterion, there is crack nucleation when the equivalent Crossland stress noted σ_c becomes higher than the torsion fatigue limit τ_d.

We can also note that for uniaxial test conditions (with a given loading ratio R), it is possible to deduce:

$$\sigma_{H,max} = \frac{\sigma_{max}}{3} \quad (5)$$

$$\sqrt{J_{2,a}} = \frac{1}{2\sqrt{3}} \sigma_{max}(1 - R) \quad (6)$$

Using these results and the fatigue limits assessed at 10^7 cycles for various R ratios, the corresponding ($\sigma_{H,max}$; $\sqrt{J_{2,a}}$) are computed (table 1) and plotted in figure 8. These data were used to approximate an equivalent "Dang Van" diagram [35-36] adapted to the Crossland formalism to establish the crack nucleation boundary.

Table 1: Compilation of the hydrostatic pressure and shear threshold values derived from fatigue limits (section 2.2)

$\sigma_{max,10^7}$ (MPA)	R	$\sigma_{H,max}$ (MPA)	$\sqrt{J_{2,a}}$ (MPA)
120	0.2	40	28
115	0.1	38	30
65	-1	22	38

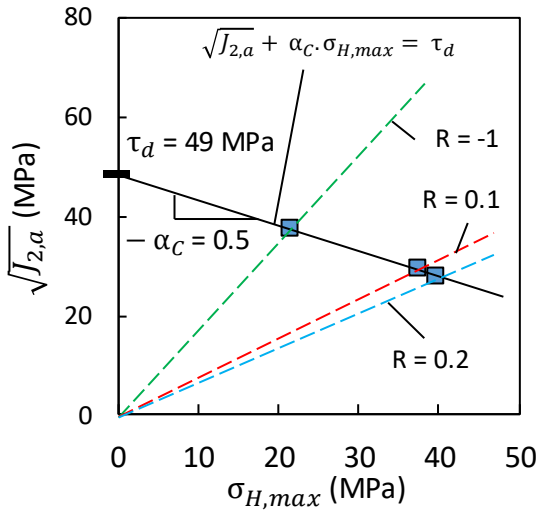

Figure 8: Plotting of the Crossland ($\sigma_{H,max}$; $\sqrt{J_{2,a}}$) diagram defining the crack nucleation boundary from plain fretting data

The three fatigue limits obtained for uniaxial tests with various loading ratios R are placed in this diagram, and the associated least squares line is plotted. The slope of this line corresponds

to $-\alpha_c$ and crosses the Y-axis at $\sqrt{J_{2,a}} = \tau_d$. This method gives $\alpha_c = 0.5$ and $\tau_d = 49$ MPa. With these results, the Crossland criterion can then be applied.

The Crossland stress σ_c is not calculated by the ABAQUS solver, so a python post-processing routine has been written to proceed to these calculations. For every single element in a predefined set located in the contact area, a value for σ_c is obtained, and the FEA output database is edited. A new artificial step is created to store the Crossland results so they can be visualized using the ABAQUS/CAE graphic interface, as shown figure 9c.

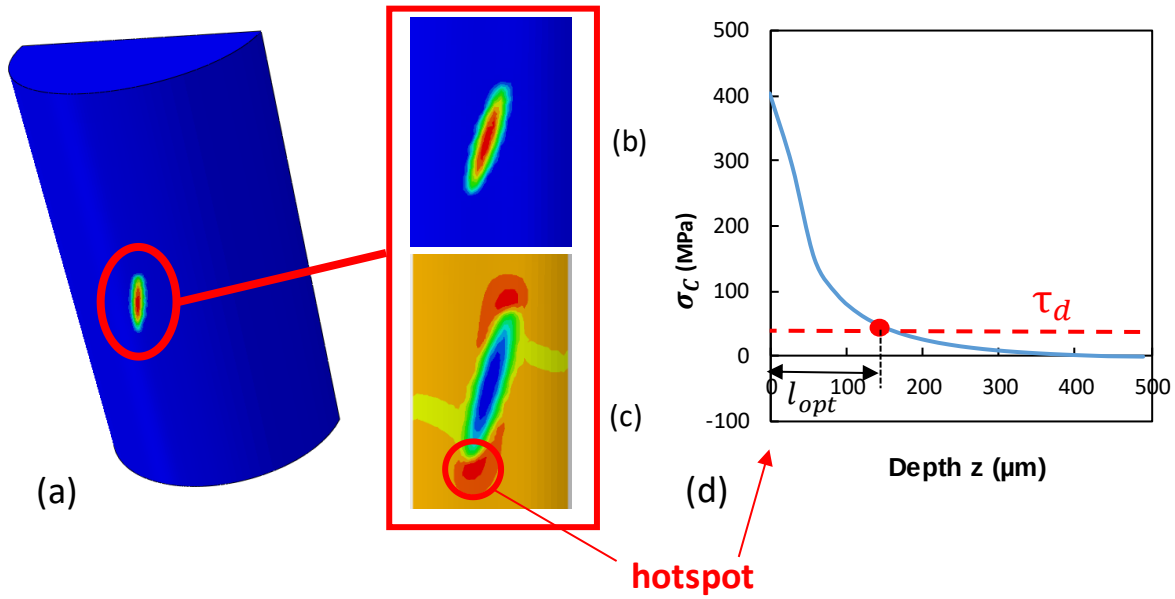

Figure 9 (a): View of a half-cylinder after simulation; (b): close-up view of the pressure distribution in the contact area; (c): close-up view of the Crossland stress distribution in the contact area; (d): Crossland stress evolution versus the depth z below the hotspot to identify the optimal critical distance l_{opt} (Q* = 75N, P = 300N)

Figure 9 shows a zoomed view of the contact area and compares the surface distribution of contact pressure (9b) and Crossland stress (9c). Figure 9c also spotlights the presence of red regions at the edges of this contact area where crack nucleation is more likely to happen. These regions are referred as “hot spots” and are critical for this local investigation on crack nucleation.

3.2.3. Identification of the optimal critical distance

The stress gradients below the hot spot induced by the contact loading is illustrated figure 9d, where the Crossland stress σ_c is plotted versus the depth z. As previously mentioned, the purpose of the non-local method used for this work is to evaluate the Crossland criterion not directly at the surface of the material, where there are the highest gradients, but beneath it. It has to be done at the optimal critical distance l_{opt}. The determination of l_{opt} is the key point of the method and is achieved by reverse identification on the plain fretting test related to the crack nucleation so that Q* = 75 N and P = 300 N (section 2.3).

As illustrated in figure 9d, the strategy to identify l implies to determine the depth below the hotspot so that the Crossland stress is equal to the shear fatigue limit:

$$\sigma_C\left(z = l_{opt}\right) = \tau_d = 49\ MPa \quad (5)$$

Considering the experimental plain fretting crack nucleation conditions (Q*=75 N, P=300 N), it leads to l_{opt} =130 µm.

A major interest of this approach is the possibility to provide a critical distance value representative of the stress gradient condition, considering that similar strand geometries and angle are imposed in the global conductor assembly. Another interesting point is the large value which is obtained. Former investigations suggest shorter critical distances from 10 and 30 µm for steel [27] and titanium [28] alloys respectively. This long critical distance may be related to the aluminium material which usually displays the longest critical distances [29]. Furthermore, as underlined by Gandiolle et al [25], plasticity influences the estimation of the critical distance. However, the proposed global-local 3D analysis of the multi-stranded conductor assembly restricts the simulations to the elastic hypothesis. Hence, the given l_{opt} = 130 µm extrapolated from the elastic simulation of the plain fretting experiment is consistent with the given numerical framework of the project. Full elastoplastic analyses should be conducted to address such a matter more accurately.

3.3. Global modeling of the conductor-clamp assembly

3.3.1. Overview

As mentioned in the introduction, wire rope structures have a complex geometry that implies a large number of contacts. The loading conditions Q*, P and δ depend on external loadings such as the mechanical tension of the conductor, the bending amplitude induced by aeolian vibrations or the clamping force. As the knowledge of these data is a key point for the current investigation, a numerical model suitable with FEA has been developed at a macroscopic scale. The purpose of this global model is to give an estimation of the contact data (fretting forces) along the axis of a clamped conductor, as represented in figure 11c.

The mesh has been generated with a MATLAB script: first a node pattern on a disk shape has been created as shown figure 10b, which is the basis of the whole mesh. This pattern features can be easily adjusted, and will define the total mesh size. Then, it is swept along various helix axes to recreate the conductor geometry with all the strands in all the layers. This way, all of the nodes coordinates are created and the next step is to define all the elements based on these nodes. The next step consists in defining the elements based on the nodes. 8-node hexahedra were used for every single strand. Eventually, this MATLAB script gives an input file that can be directly imported in the ABAQUS CAE interface to complete the model and run calculations.

As it is intended to specifically focus on the conductor, the whole clamping system (keeper + clamp support) has been modeled using shells (figure 10c.) rather than solid elements to reduce the computational cost. However, given the large amount of contacts bringing non-linear phenomena in an already heavy representation, this model is not suitable for implicit calculations. Thus, the dynamic explicit solver from ABAQUS has been used at this scale.

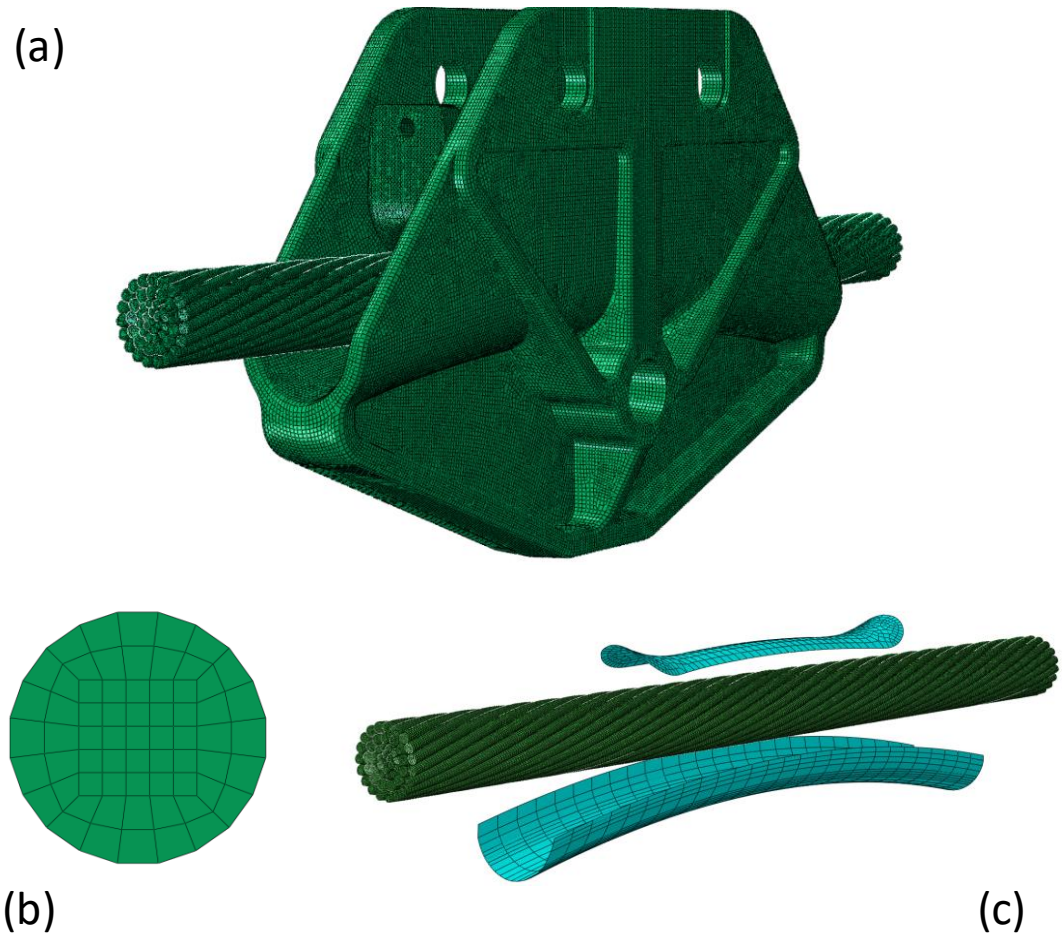

Figure 10 (a): Global view of the total meshing using hexaedrla solid elements for the conductor-clamp assembly; (b): nodal pattern used to mesh each strand of the conductor; (c): view of lighter mesh assembly where the clamp is modeled using shell elements

3.3.2. Contact data post-processing

Besides stress and strain results available at each node or element in the output database, the solver also gives contact data such as contact pressure or reaction forces. However, further fretting analyses do not require nodal values but integrated forces on a whole contact. To achieve that, a python routine has been written to post-process any output database obtained from the global model. This routine scans all surface nodes and, whenever there is a non-zero value for the reaction force magnitude, a "contact instance" is created. Then, all the neighboring nodes are checked, and other non-null nodes are added to the current instance. This way, all contacts between the two aluminum layers can be fully reconstructed and mapped along the axis. For every single contact detected between the two aluminum layers, the following values are calculated:

- The reaction force vector $\vec{R}$ (3 components)
- The scalar *P*, the force normal to the contact surface, which is the projection of $\vec{R}$ on the normal axis of the contact.
- The tangential force vector $\vec{Q}$ which is a projection of $\vec{R}$ on the tangential plane and its norm $Q^* = \|\vec{Q}\|$
- The scalar ratio $\frac{\|\vec{Q}\|}{\|\vec{P}\|}$
- The centroid coordinates (3 components)

The knowledge of these data allows to map all the contacts along the conductor with their location, their intensity and most importantly their projections Q* and P.

3.3.3. Computation for a reference bending fatigue loading

The following results have been obtained for a theoretical case with realistic loadings that can be found on conductors on the grid. However, some of these shall be improved with more accurate estimations, especially related to the clamping effort and the link between aeolian vibrations and bending amplitude. As it is not the topic of the current study, the numerical method remains the same.

The boundary conditions applied on the model are the following:

- The portion of conductor modeled has a total length of 400 mm
- One end of the conductor is fixed
- The other is bent with an angle of 11° with respect to the horizontal position. This specific value comes from observations made on the French grid
- A mechanical tension of 30 kN is applied
- The clamping is obtained with a total pinch of the conductor of 1mm

Figure 11b shows the 3D spatial distribution of all the detected contacts within a conductor in its bent position. Each point corresponds to the centroid of a contact. The distribution of the normal loads associated with these same contacts is also represented in figure 10c. The clamping influence is clearly put in relevance in the area between 100 and 300 mm with the appearance of highly loaded contacts. This kind of plot can be made for the tangential force as well, as shown figure 12a.

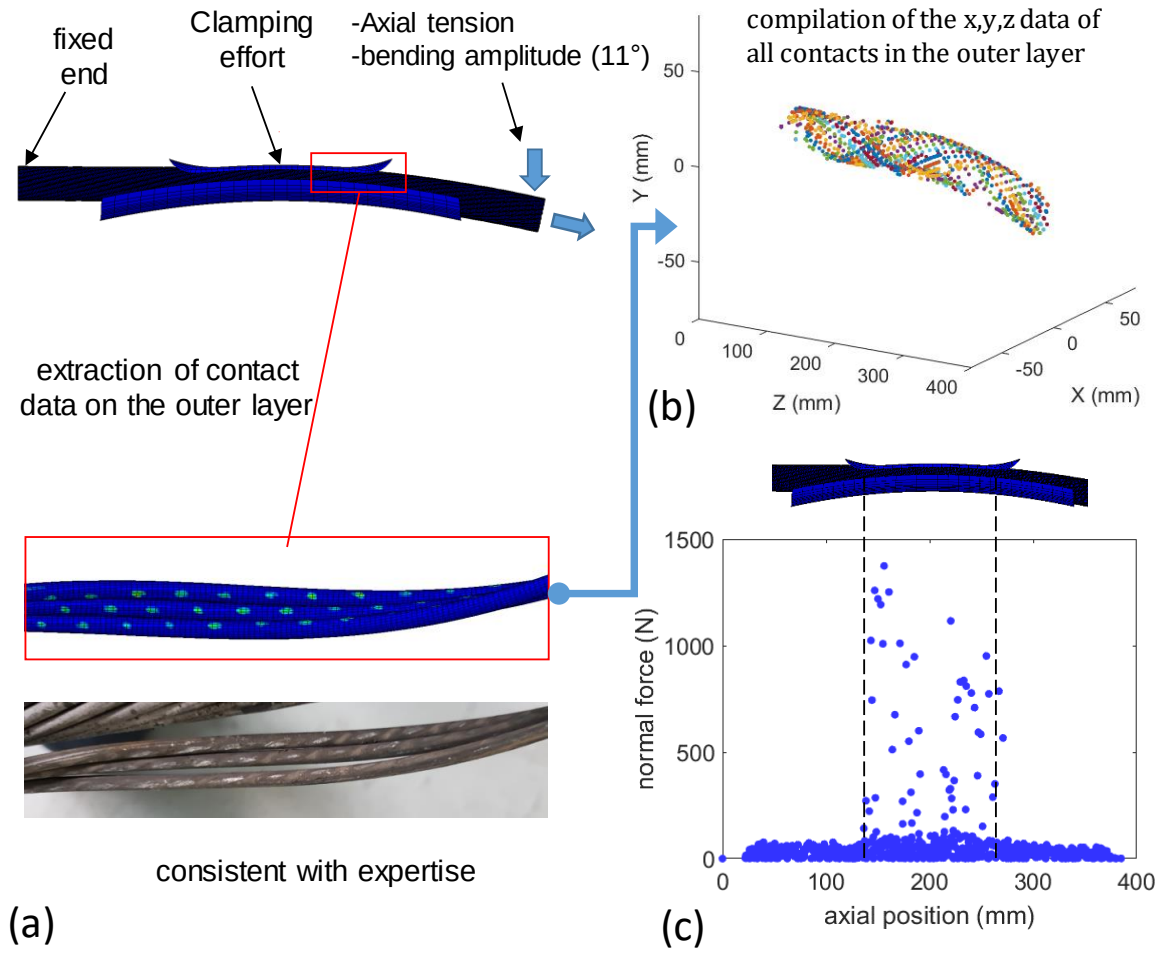

Figure 11: (a) Illustration of the reference case with a close-up view of the contacts detected in the outer layer; (b) 3D mapping of the centroids of inter-strand contacts for the outer layer. (c) axial distribution of the normal forces associated with each contact detected (30 kN of total axial tension, 11° bending amplitude)

All these contacts can be sorted according to the main parameters related to fretting and fatigue damage: the tangential load Q* and the maximum fatigue bulk stress $\sigma_{f,max}$. Table 2 shows the spread of such sorted contacts. From this figure emerge three relevant categories to investigate:

- (1): Contacts with low fretting loading (Q* < 30 N) and high fatigue stress ($\sigma_{f,max}$ >80 MPa). The majority of contacts detected by the post-processing routine enters this category with more than 400 instances.

- (2): Contacts with intermediate fretting loading (30 N < Q* < 150 N) and (30 MPa < $\sigma_{f,max}$ < 80 MPa). These instances are located within the clamping zone.

- (3): Contacts with high fretting loading (Q* > 150 N) and low fatigue ($\sigma_{f,max}$ < 30 MPa). These instances are located in the clamping zone as well.

Table 2: Distribution of the number of contacts detected according to the fatigue loading $\sigma_{f,max}$ and the fretting loading Q*

Q* / $\sigma_{f,max}$	$Q^* < 30$ N	$30\ N < Q^* < 150\ N$	$Q^* > 150\ N$
$\sigma_{f,max} < 30\ MPa$	126 contacts	35 contacts	18 contacts (3)
$30\ MPa < \sigma_{f,max} < 80\ MPa$	232 contacts	12 contacts (2)	0
$\sigma_{f,max} > 80\ MPa$	401 contacts (1)	0	0

The proposed method implies to select some specific contacts for further investigations, thus two contacts for each category were picked in order to account for as many cases as possible. Contacts 1 and 6 belong to category (1), 2 and 5 to category (2) and the two remaining 3 and 4 belong to category (3). These six contacts are displayed on figure 12: figure 12a illustrates how they were picked based on their tangential load along the conductor axis, and figure 12b also shows the normal load for these

specific contacts. Eventually, figure 12c focuses on the fatigue stress by representing their maximum bulk stress $\sigma_{f,max}$.

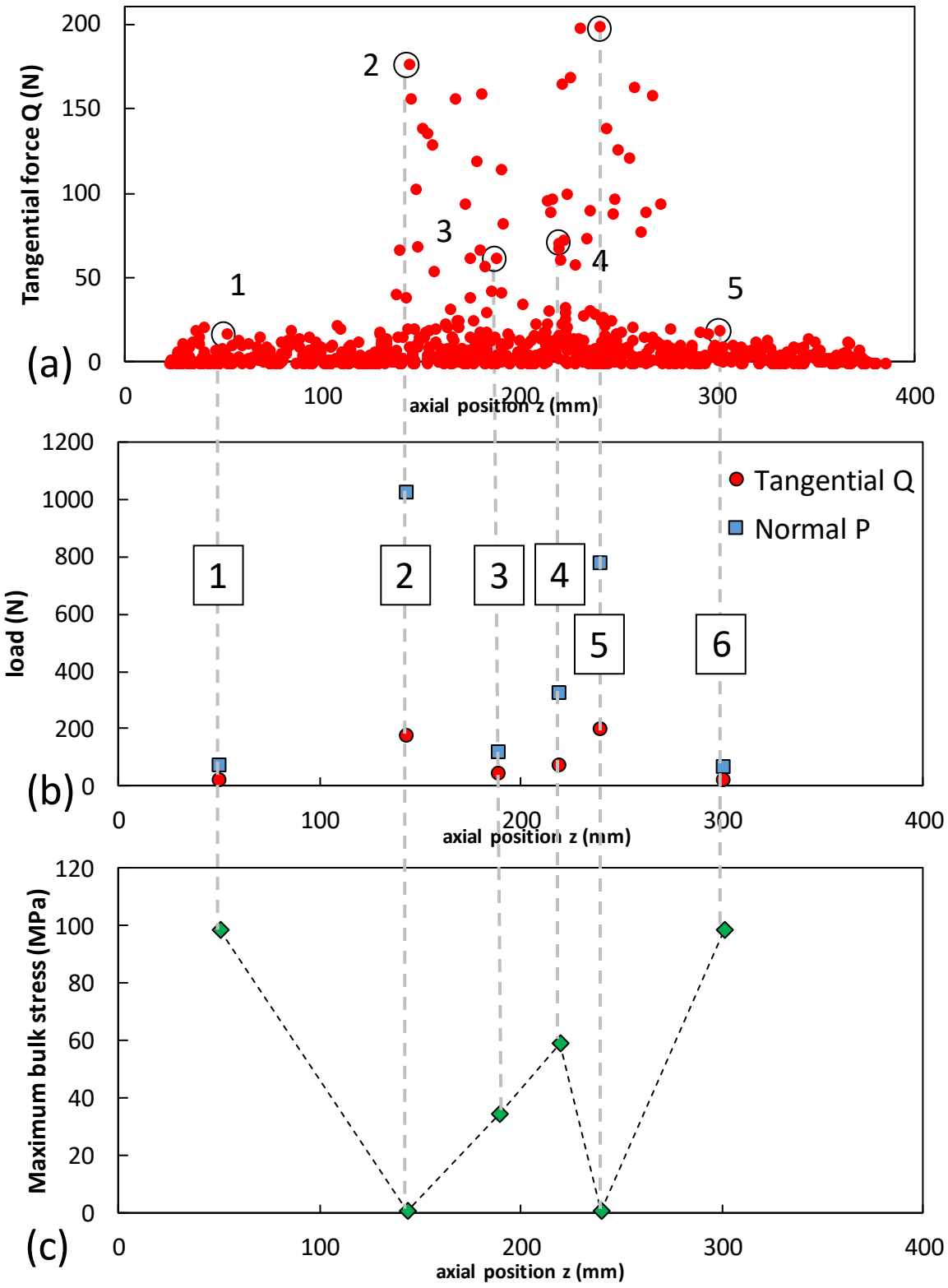

Figure 12 (a): Axial distribution of the tangential loads associated with contacts on the outer layer and outline of the 6 contacts retained for further investigations; (b) display of the tangential Q* and normal P loads of these 6 loading cases; (c) Corresponding fatigue stress amplitudes along the conductor axis

Table 3: Description of the six loading cases selected. Red: σ_c/σ_d >1 (crack nucleation); blue: σ_c/σ_d <1 (no crack nucleation).

LOADING CASE	P (N)	Q* (N)	$\sigma_{f,max}$ (MPA)	$\frac{\sigma_C(HS)}{\tau_d}$	$\frac{\sigma_C(l_{opt})}{\tau_d}$
1	71	17	99	3.4	0.6
2	1024	176	4	9.2	2.5
3	117	41	35	5.5	1.2
4	320	70	60	6.86	1.05
5	777	199	3	10.61	2.2
6	64	18	98	3.5	0.8

With these data in hand, the next step of the method consists in switching scale in order to focus on a single contact fretting fatigue and use these fatigue and fretting loadings as input for the next model.

Hence, as for the plain fretting investigation, the fretting fatigue stress paths were computed using the mono-contact local model as described in figure 8. However, in addition to the constant normal loading P and the alternated tangential fretting force ±Q*, a fatigue loading $\sigma_{f,max}$ is also imposed to the lower specimen with a fatigue stress ratio R = 0.5. For each loading cases compiled in table 3, the Crossland stress is computed on the surface to detect the hotspot stress σ_c(HS) location (usually observed at the trailing contact edge). Then the Crossland stress computed at z = l_{opt} = 130 µm vertically beneath the hotspot location is extracted and considered for the non-local cracking risk analysis. Using this basic strategy, the stress gradient effects are taken into account and better predictions (i.e. less conservative) are expected.

Figure 13a compares the σ_c(HS) stress values for the selected loading cases. Whatever the situation, the hotspot stress analysis predicts crack initiation, with $\sigma_c(HS)/\tau_d > 1$. This result is quite unexpected as no crack were never observed in the outer regions of the clamping assembly, i.e. loading cases 1 and 6.

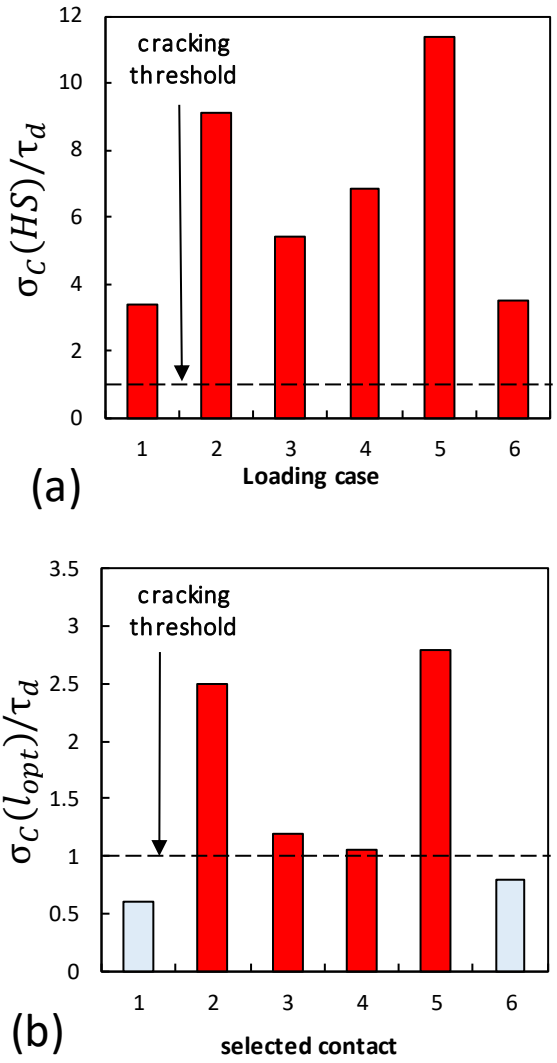

Figure 13: Crack nucleation risk assessed with the Crossland criterion for the 6 loading cases considered. (a) using $\sigma_C(HS)$ evaluated directly at the hotspot surface; (b) using $\sigma_C(l_{opt})$ evaluated at the optimal critical distance found section 3.2.2.

The non-local fatigue stress analysis leads to different conclusions. Figure 13b shows that when considering $\sigma_c(l_{opt})$, contacts 2, 3, 4 and 5 may suffer crack nucleation within 10^7 cycles while contacts 1 and 6 may not. Other contacts could be tested using the same procedure in order to check the crack nucleation risk depending on Q*, P, the maximum bulk stress $\sigma_{f,max}$ and the loading ratio *R*. More generally, it can be stated that all contacts from category (1) won't nucleate. On the contrary, due to the high fretting loads, the Crossland criterion would overpass the cracking threshold for contacts in category (3). At last, contacts from category (2) may have distinct Crossland criterion results above and below the cracking threshold.

An interesting aspect of this post-processing non local fatigue stress analysis is the rather good correlation with aged conductor observations. It predicts well that most of the fretting damage is located on both edges of the clamp (contacts 2 and 5) while there is a lower risk at the center of the assembly (contact 3) and especially outside of the clamping zone (contacts 1 and 6). These results match with results from literature and recorded observations from the french power grid.

4. Mono contact fretting fatigue tests

To validate the given global-local $\sigma_c(l_{opt})$ predictive strategy it would be interesting to perform macroscopic bending tests on an actual conductor-clamp assembly. However, such tests are very expensive and require dedicated infrastructures [31, 32]. An alternate strategy consists in performing mono-contact fretting fatigue tests applying loading conditions similar to those predicted in the conductor-clamp assembly. This required the use of a former double actuator test bench coupled with a newly designed system in order to be compatible with low loading contact conditions.

As represented in figure 14a, the fretting fatigue experimental tests use two hydraulic actuators: a first one to apply a fatigue loading on the fatigue sample, and a second one to apply a displacement on the fretting samples, in order to induce fretting at the contact. In practice, the fatigue sample undergoes two contacts related to two distinct fretting samples as shown in figure 14b.

Like plain fatigue tests, a special attention has been given to the way the fatigue sample was restrained in order to avoid jaw located failures. However, using the same reshaped samples as for plain fatigue was not a considerable option: removing material at the surface would affect the tribological response of the strands, which is a key aspect of any fretting test. Four half cylinders were designed, two for each end of the fatigue sample. The roughness of their inner surfaces was enhanced with abrasive blasting, and a compromise was found on the clamping pressure so the failure would happen in the fretting area and nowhere else.

Fatigue $\sigma_f(t)$ is applied on the fatigue sample using the lower actuator and is force controlled through the load measured by sensor 1 on figure 14. Fretting is obtained by imposing and controlling the displacement $\delta(t)$ of the upper actuator, and the tangential force Q(t) is calculated as the difference between the forces measured by sensor 1 and sensor 2. The displacement setpoint is progressively adjusted until the tangential force amplitude Q* reaches its targeted value. Then, as long as the contact remains in partial slip and the displacement amplitude is kept constant, Q* is stable throughout the test.

For every test, the targeted lifetime was set at 10^7 cycles to be consistent with the fatigue limit assessed with the plain fatigue tests. It means that if a sample did not break within 10-12 million cycles, the test would be stopped in order to process the unfailed strand using destructive analysis and crack length measurements.

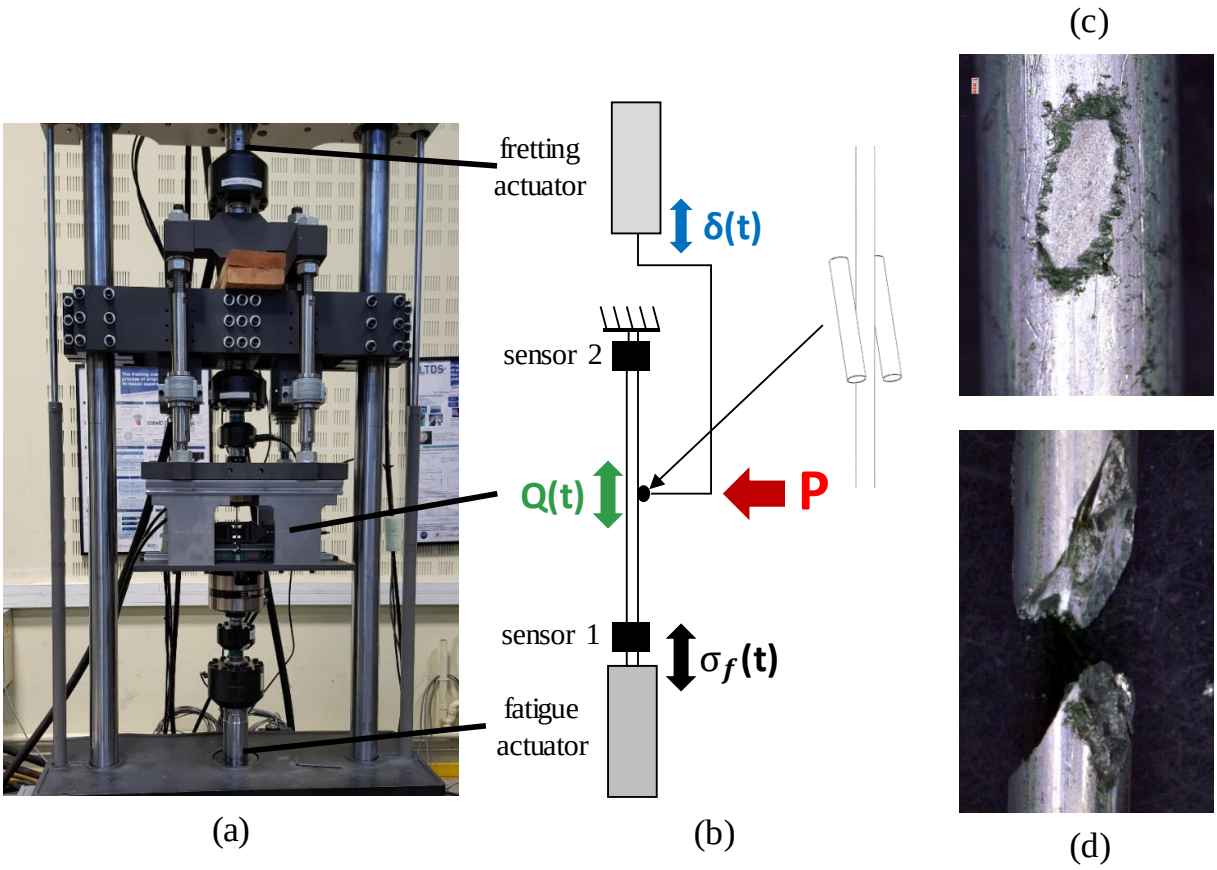

Figure 14 (a): Double actuator device used for fretting fatigue mono-contact tests; (b) schematic drawing of the double actuator device; (c) optical view of the fretting scar on an unfailed strand (Q*= 80 N, P = 300 N, $\sigma_{f,max} = 40\ MPa$ and R = 0.5); (d) optical view of a failed strand (Q* = 150 N, P = 200 N, $\sigma_{f,max} = 60\ MPa$ and R = 0.5)

Several fretting-fatigue tests were conducted in order to reproduce loadings extracted from the global model that have been used as input for the local model. These first experimental results would then be compared with the crack nucleation risk established for the five selected contacts highlighted in previous sections. Among these six specific contacts and according to the Crossland criterion (figure 13), contacts 1 and 6 are not expected to fail or even display crack nucleation. On the contrary, contacts 2, 3, 4 and 5 are expected to nucleate, thus to fail within 10^7 cycles given the initial hypothesis associating crack nucleation with failure.

The main conclusion arising from these mono-contact fretting fatigue tests is that this hypothesis may not be sufficient to predict the total failure of a strand. None of the tests achieved to reproduce simulated contacts broke before reaching 10^7 cycles. However, the use of a multiaxial fatigue criterion

to predict crack nucleation remains relevant, as the destructive analysis of the tested samples revealed the presence of cracks below contact areas. For contacts 1 and 6, the average crack length remains below 40 µm, while it gets higher than 50 µm for contacts 2, 3, 4 and 5 for which $\sigma_c(l_{opt})/\tau_d > 1$. It can be noted that the $\sigma_c(l_{opt})$ crack nucleation model was calibrated for a 50 µm projected crack length. Therefore, it can be concluded that the given $\sigma_c(l_{opt})$ predicts well the fretting fatigue crack nucleation risk but not the total failure risk which may require to consider propagation mechanisms. For example, even if contacts 2 and 5 from category (3) display the highest values for the Crossland criterion σ_c/τ_d, the very low fatigue loadings associated with these cases imply a rather low probability of failure. With less than 5 MPa of maximum bulk stress, they are closer to plain fretting conditions than fretting fatigue conditions. In a similar manner, contacts from category (1) are closer to plain fatigue conditions than fretting-fatigue.

To highlight the link between the cracking processes and the nucleation risk assessed in this method, more fretting-fatigue tests were achieved to investigate the behavior of fretting induced cracks, with solicitations corresponding to category (2). Then, for each of these tests, the associated Crossland criterion was calculated using the local model such as described section 3.2. Figure 15 shows three pictures corresponding to three distinct values for the Crossland criterion. In addition to these images, figure 16 displays more crack depths versus the associated criterion and a quasi-linear evolution of the crack depth is observed. These results illustrate the relevance of the $\sigma_c(l_{opt})$ criterion to predict crack nucleation, even in fretting-fatigue: this approach predicts well the fretting-fatigue crack nucleation condition (i.e. $\sigma_c(l_{opt}) = 1$ with b = 50 µm) even though the l_{opt} methodology was calibrated using very different plain fretting experiments.

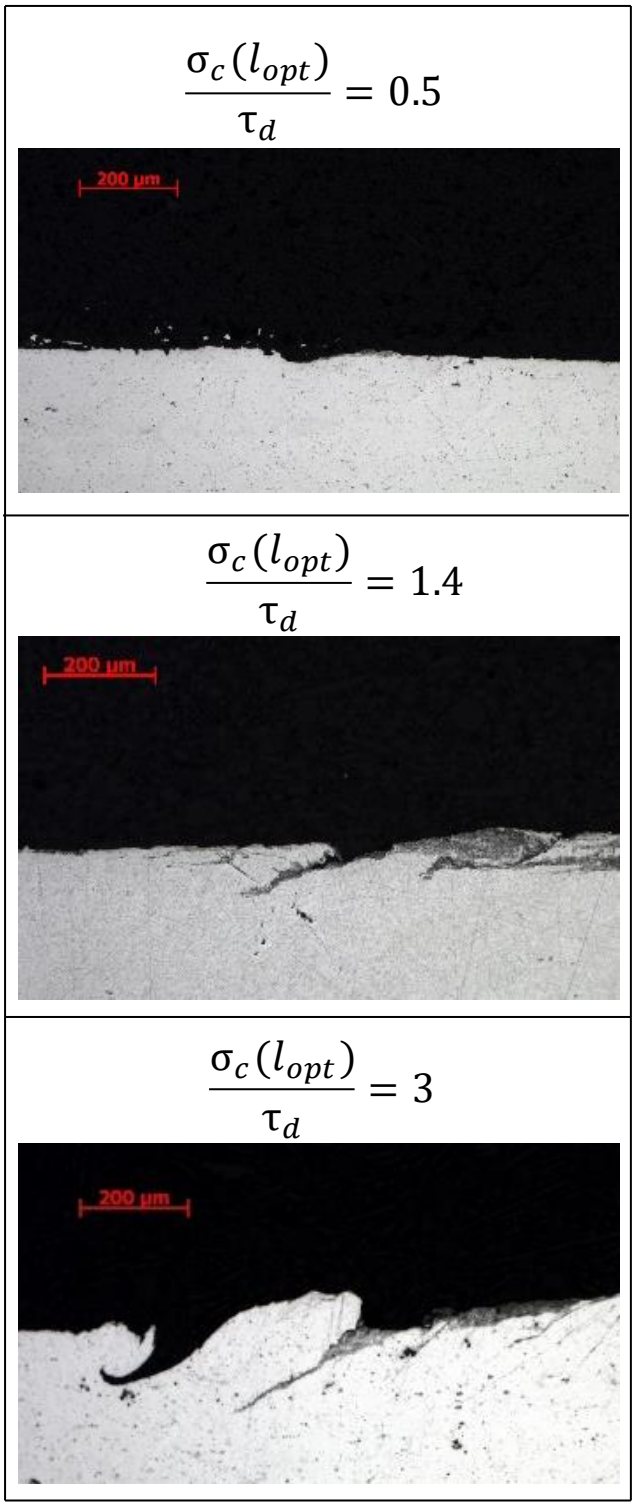

Figure 15: cross-sectional views of the contact zones for 3 distinct loading conditions, with the associated $\frac{\sigma_c(l_{opt})}{\tau_d}$ ratio

Table 4: Mono-contact fretting-fatigue experiments (10^7 cycles, β = 30°)

P (N)	Q* (N)	$\sigma_{f,max}$ (MPA)	b (µm)
64	18	100	**30**
100	35	70	**45**
310	70	70	**80**
310	125	70	**175**
310	150	70	**210**
310	200	70	**300**

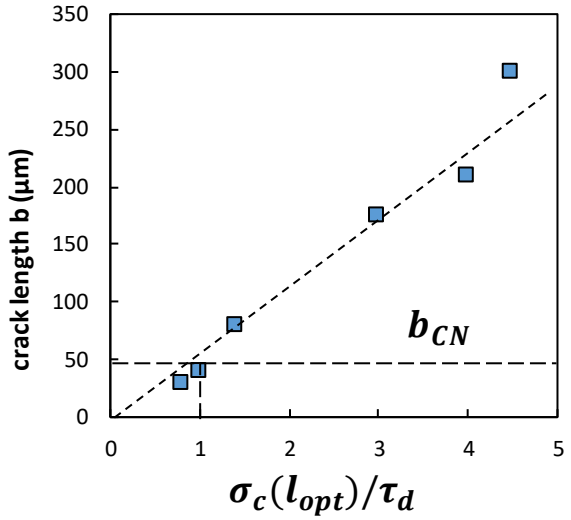

Figure 16: Crack depth in fretting-fatigue after 10^7 cycles as a function of the Crossland criterion for the tests displayed table 4

To complete these observations, some additional tests were conducted with high fretting loads (Q* > 150 N) and medium fatigue load (30 MPa < $\sigma_{f,max}$ <80 MPa). For these specific cases, the associated criteria were high with $\sigma_c(l_{opt})/\tau_d > 3$ and total failures were observed before 10^7 cycles. However, as showed on table 2, such heavily loaded contacts were not detected for the reference case computed section 3.3.3.

In the light of all of these elements, it appears crucial to consider longer lifetimes to apprehend the whole cracking process properly. The reference case studied in this work is already conservative: there

is no electrical conductor suffering such a tensile load with a bending angle higher than 10°. This choice was made to increase the chances to witness total failures within a reasonable testing time, as the hydraulic actuators used are limited to 20 to 30 Hz in fretting-fatigue configurations. Thus, longer experiments with tests reaching 10^8 would be the natural next step of investigation: it would allow to verify whether the cracks nucleated within the 10^7 cycles are likely to propagate or not. These cracks may also reach their crack arrest conditions for some loadings, and longer experimental tests would be a reliable way to assess this phenomenon.

Still, this simplified plain fretting "post-processing" $\sigma_c(l_{opt})$ strategy presently validated to predict fretting fatigue crack nucleation appears to be a relevant and reliable safe-cable designing strategy. It provides conservative damage predictions which, whatever the remaining propagation lifetime, stands as the main objective of any industrial designing tool.

5. Numerical crack arrest investigations using Zcracks

As a first attempt to investigate the propagation behavior of fretting induced cracks numerically, the Zcracks module has been used applied on the local model presented section 3.2.1. Zcracks is a module from the Z-set suite that is dedicated to crack propagation studies in 3D configurations. Among all the tools offered by Zcracks, the two following have been exclusively used for the results presented in this section [33]:

- The remeshing tool that allows to insert a surface geometry (user-defined) into a "sane" mesh to model the presence of a crack. The remeshed model uses only tetrahedral volume elements with a refined mesh located along the crack tip. Figure 17 illustrates how the local model initial mesh is affected by this operation.

- The post-processing tool computing the distribution of Stress Intensity Factor (SIF) from Linear Elastic Fracture Mechanics (LEFM) along the crack tip. K_I, K_{II} and K_{III}, associated

with mode I, II and III respectively, are thus calculated for several points on the crack tip. The mode I equivalent SIF K_{eff} is also obtained, as defined in equation (7).

In linear elasticity, the post-processing calculations are based on the energy release rate G at a point of the crack tip, which is related to the SIFs according to the IRWIN relation:

$$G = \frac{1-\nu^2}{E}\,(K_I^2 + K_{II}^2) + \frac{K_{III}^2}{2\mu}, \quad \text{with } \mu = \frac{E}{2(1+\nu)} \tag{6}$$

Finally, G is computed using the G – theta method [33-34], and the mode I equivalent SIF K_{eff} is given by:

$$K_{eff} = \sqrt{\frac{E.G}{1-\nu^2}} \tag{7}$$

It should also be mentioned that whenever $K_I < 0$, the equivalent K_{eff} is systematically equal to zero. Then, K_I, K_{II} and K_{III} can be obtained by introducing any pure mode I, II or III Westergaard displacement solutions $v^{I,\,II,\,III}$, associated with the corresponding release rates $G^{v,I,\,II,\,III}$:

$$K_I = \sqrt{\frac{E}{1-\nu^2}\,G^{v,I}} \tag{8}$$

$$K_{II} = \sqrt{\frac{E}{1-\nu^2}\,G^{v,II}} \tag{9}$$

$$K_{III} = \sqrt{2\,\mu\,G^{v,III}} \tag{10}$$

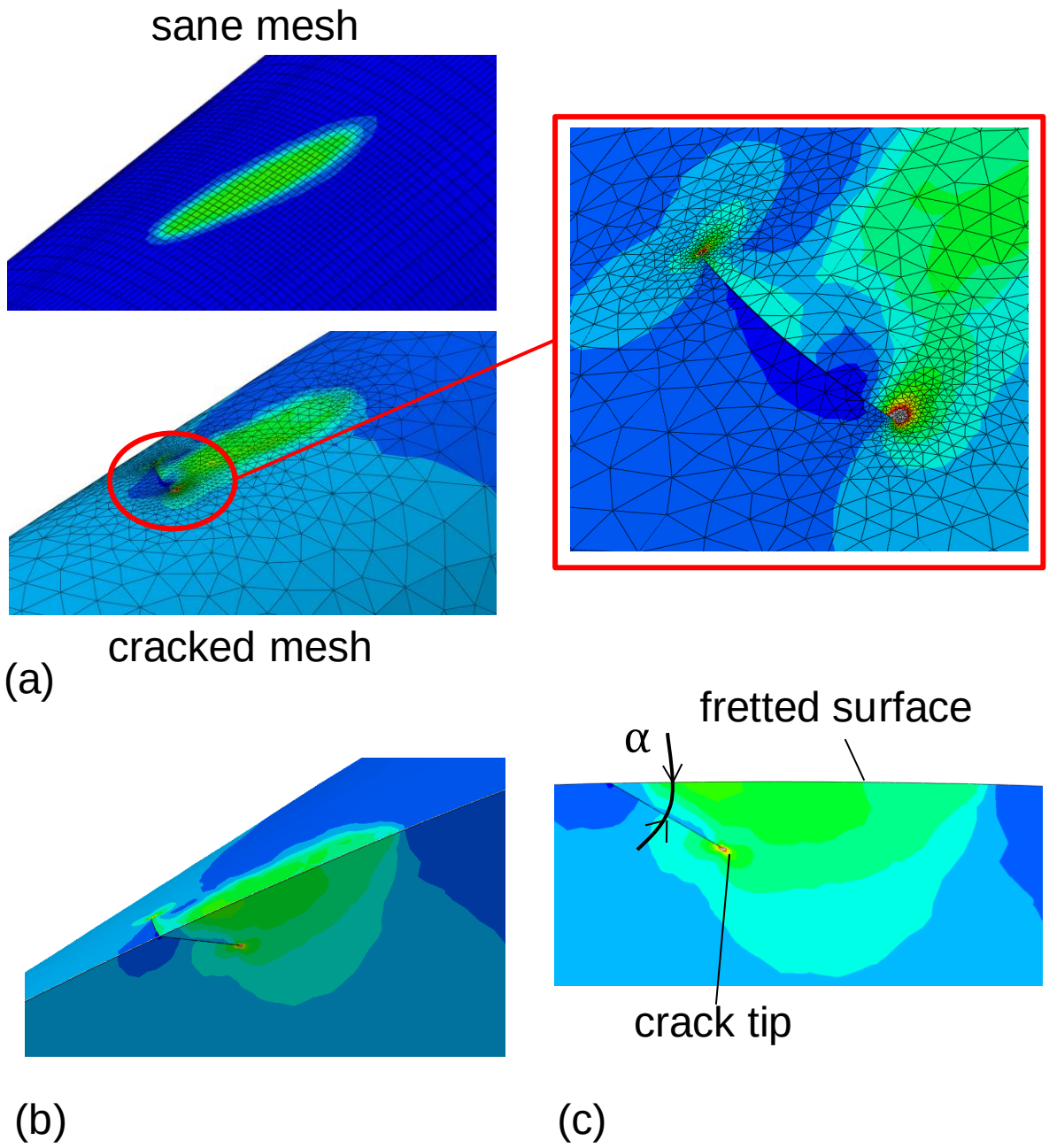

Figure 17 (a): comparison between the sane mesh and cracked mesh with a close-up view of the inserted crack at the surface; (b): tilted cross-sectional view of the contact area after calculation; (c): cross-sectional of the contact area showing the definition of the angle α used to characterize the inserted crack orientation

The use of Zcracks was motivated by experimental observations concerning crack shapes: for both failed strands (figure 14d) or unfailed strands (figure 5, figure 15), cracks systematically display a low diving angle α (defined figure 17c) about 30°. This is believed to be related to the microstructure of the studied material induced by the manufacturing process. The aluminium strands are obtained by

wire drawing, which deeply affects the microstructure. It also known to induce significant residual stress, although this aspect will not be considered here.

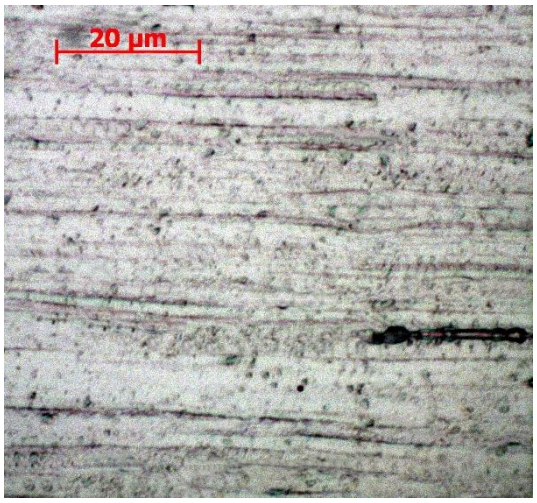

Figure 18: optical view of the aluminium microstructure emphasized using Keller's reagent. The axis of the strand is horizontal.

Figure 18 displays the microstructure of the studied material, where the grain boundaries share the same direction with the strand itself. As a result, a nucleated crack would have to cross more grain boundaries when the angle α increases. This may explain the experimental observations where cracks tend to follow the general direction of these material features. This geometrical effect associated with the hydrostatic pressure induced by the normal force in a fretting contact may also explain the crack arrest phenomena observed in fretting fatigue experiments. However, further investigations would be required to explain these experimental crack inclinations. Residual stresses and some outplane propagation criteria are likely to give potential answers. Still, the following results are meant to highlight the influence of these geometrical features, based on experimental shapes.

The procedure used to proceed to the calculations on cracked meshes consists in the following steps:

- The sane model is defined in the ABAQUS/CAE interface with all the relevant boundary conditions. A static normal force P=75 N or 150 N is imposed coupled with a cyclic tangential

force Q(t) = ± 50 N. Similarly, a cyclic bulk stress $\sigma_f(t)$ = 60 MPa ± 40 MPa is applied to describe a single cycle. Then the input file is generated.

- The ABAQUS input file is imported in the Zcracks interface.

- An elliptical crack shape is inserted into the initial sane mesh. The location and shape are user-defined based on experimental observations on the hotspot location. Three diving angle were tested for the crack orientation: α=30°, 45° and 60°. For each case, the crack was manually propagated without any bifurcation.

- The new model is remeshed to embed the newly defined crack.

- A new ABAQUS input file is generated by Zcracks and submitted to the solver for calculations

- The output database is processed by the Zcracks SIF computing routine to get the SIF values at the crack tip.

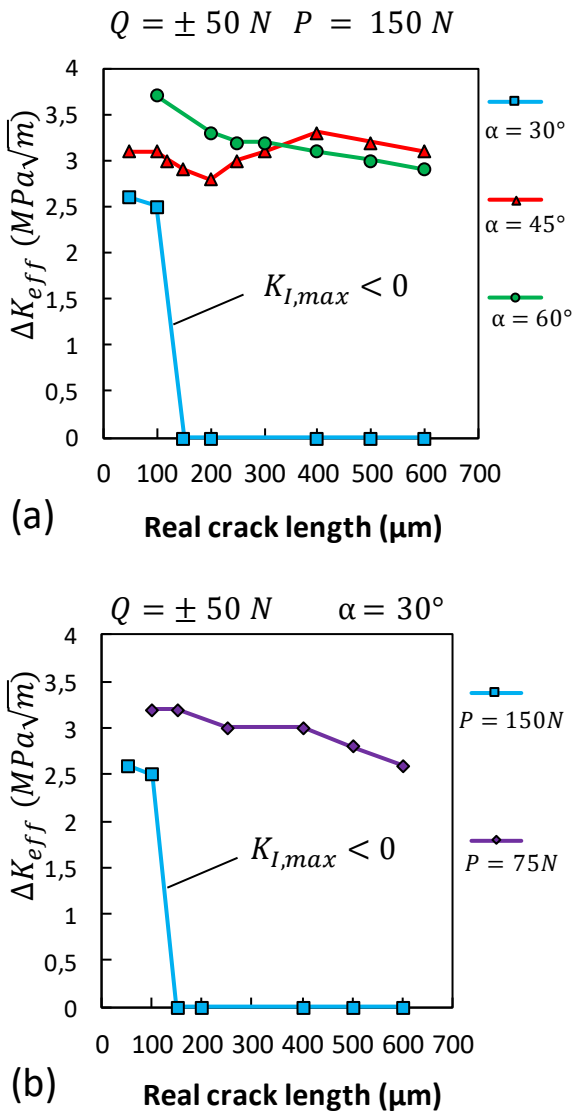

Figure 19 (a): ΔK_{eff} evolution versus the real crack length for various diving angles (Q*=50 N and P=150 N); (b): ΔK_{eff} evolution versus the real crack length for two distinct normal force (Q* = 50 N and α=30°)

Figure 19 displays the results obtained following the previous procedure by plotting the ΔK_{eff} (at the endpoint of the crack) which drives the crack propagation versus the total length of the crack. Figure 19a focuses on the influence of the crack orientation, kept constant as the crack propagates. The case for which α = 30° corresponds to the real orientation observed on experimental samples, while α = 45° and α = 60° correspond to usual angles observed for other materials. As shown on figure 19a, it is interesting to note that for these higher angles (45° and 60°), ΔK_{eff} remains higher than 3 MPa.m$^{1/2}$ whatever the crack length. Hence, for such crack angle conditions, the crack nucleation will systematically lead to failure. This confirms the conventional correlation between crack nucleation

computation and fretting endurance predictions. On the other hand, for the studied $\alpha = 30°$ condition corresponding to experimental observations, ΔK_{eff} drops to zero before reaching 150 µm, inducing the crack arrest condition. Hence, using such a 3D crack propagation analysis, it is possible to explain why for the studied material, the sole crack nucleation modeling cannot fully allow the prediction of fretting-fatigue failure. Furthermore, figure 19b illustrates the effect of the normal force. The interesting result is that by increasing the normal force for the same tangential force Q*, the compressive hydrostatic stress is also rising and therefore the crack arrest condition is favored.

6. Conclusion

The present study proposes a numerical and experimental method to assess the behavior of an ACSR electrical conductor under fretting-fatigue solicitations. Two distinct numerical models were developed, and various types of experimental testing were conducted to support this modeling work. The following points were exposed:

- Plain fretting tests were achieved to characterize the tribological response of an aluminium/aluminium contact between two strands and determine the transition parameter μ_t required in the global model. These tests were also used for the post-processing identification of the optimal critical distance used with the Crossland criterion, giving l_{opt} = 130 µm.

- A global model has been used to represent at a macroscopic scale a whole portion of conductor and an associated clamp. This tool allows to evaluate the fretting and fatigue loading undergone by a bent conductor and all the strands that composes it. The consideration of this global scale is required to account for the high influence of geometry in a wire rope assembly.

- To complete these global assessments, the problem has also been addressed at a local scale by modeling a single contact between two aluminum strands. This numerical inter-strand contact is used to evaluate the crack nucleation risk using an Elastic-Crossland computation, combined with a non-local Critical distance $\sigma_c(l_{opt})$ method. This computation was calibrated beforehand with simplified plain fretting experiments (i.e. ECFD approach). An optimized strategy was defined to select 6 representative loading cases along the conductor/clamp assembly.

- Comparison between the non-local $\sigma_c(l_{opt})$ approach and the σ_c(HS) hotspot stress analysis confirms that the non-local $\sigma_c(l_{opt})$ provides more realistic predictions. $\sigma_c(l_{opt})$ predicts crack

mostly at the edges of the clamping assembly, while no damage is expected outside the clamp as it can be anticipated from observations on aged conductors. σ_c(HS) on the other hand, overestimates the cracking risk and predict cracking failure for every contacts.

- A dedicated fretting-fatigue test bench with hydraulic actuators was designed in order to recreate the same conditions than those issued from the numerical global model. Those tests revealed the relevance of the ECFD strategy to predict the crack nucleation within 10^7 cycles. All the selected loading cases for which $\sigma_c(l_{opt})/\tau_d > 1$ display crack lengths longer than b_{CN}=50 µm at the crack nucleation threshold. This good correlation to predict the fretting fatigue crack nucleation risk was confirmed by plotting the evolution of the crack depth b versus $\sigma_c(l_{opt})/\tau_d$ for various loading cases.
- However, if the given "plain fretting post-processing" optimization of the non-local $\sigma_c(l)$ model predicts well the crack nucleation risk, it is not fully capable to capture the complete failure risk.
- A preliminary study using Zcracks has been performed to illustrate the possibility of crack arrest implied by hydrostatic pressure effects.

A major interest of the given global-local ECFD approach is the ability to provide reliable predictions of crack nucleation for such complex assemblies as those used by any TSO. This appears as an interesting tool for future optimization of conductor/clamp assemblies or to predict damage location on already installed power lines. Further scientific developments are now undertaken to address the effect of plasticity, perform more crack propagation investigations and develop new high frequency fretting fatigue tests to address long range 10^8 cycles fretting fatigue endurances.

Reference

[1] **R. E. Hobbs, M. Raoof**, *Mechanism of fretting fatigue in steel cables*, Int. J. Fatigue, 16 (1994) 273-280

[2] **W. Fricke, C. Rawlins**, *Importance of fretting in vibration failures of stranded conductors*, IEEE Transactions on Power Apparatus and Systems, PAS-87 (1968) 1381-1384

[3] **V. F. Steier, R. B. Kalombo, C. da Silva, M. Nogueira, J. A. Araùjo**, *Effect of chromium nitride coatings and cryogenic treatments on wear and fretting fatigue resistance of aluminium*, Electric Power Systems Reasearch 116 (2014) 322 – 329

[4] **R. B. Kalombo, J. A. Araùjo, J. L. A. Ferreira, C. R. M. da Silva, R. Alencar, A .R. Capra**, *Assessment of the fatigue failure of an All Aluminium Alloy Cable (AAAC) for a 230 kV transmission line in the Center-West of Brazil*, Engineering Failure Analysis 61 (2015) 77 – 87

[5] **A. A. Fadel, D. Rosa, L. B. Murça, J. L. A. Ferreira, J. A. Araùjo**, *Effect of high mean tensile stress on the fretting fatigue life of an Ibis steel reinforced aluminium conductor*, Int. J. Fatigue 42 (2012) 24-34

[6] **G. Chen, X. Wang, J. Wang, J. Liu, T. Zhang, W. Tang**. *Damage investigation of the aged aluminium cable steel reinforced (ACSR) conductors in a high-voltage transmission line*, Engineering Failure Analysis 19 (2012) 13-21

[7] **G. E. Ramey, J. S. Townsend**, *Effects of clamps on fatigue of ACSR conductors*, Journal of the Energy Division, Proceedings of the ASCE 107 (1981) 103-119

[8] **A. Cardou, L. Cloutier, J. Lanteigne, P. M'boup**, *Fatigue strength characterization of ACSR electrical conductors at suspension clamps*, Electric Power Systems Research, 19 (1990) 61-71

[9] **Z. R. Zhou, A. Cardou, S. Goudreau, M. Fiset**, *Fretting fatigue in electrical transmission lines*, Fatigue Fract. Eng. Mater. Struct. 173 (1994) 179-188

[10] **Z. R. Zhou, S. Goudreau, M. Fiset, A. Cardou,** *Single wire fretting fatigue tests for electrical conductor bending fatigue evaluation*, Wear 181-183 (1995) 537-543

[11] **Z. R. Zhou, A. Cardou, S. Goudreau, M. Fiset,** *Fretting patterns in a conductor-clamp contact zone*, Fatigue Fract. Eng. Mater. Struct. 17 (1994) 661 – 669

[12] **A. Cruzado, M. A. Urchegui, X. Gomez**, *Finite element modeling and experimental validation of fretting wear scars in thin steel wires*, Wear 289 (2012) 26 – 38

[13] **A. Cruzado, S. B. Leen, M. A. Urchegui, X. Gomez**, *Finite element simulation of fretting wear and fatigue in thin steel wires*, Int. J. Fatigue 55 (2013) 7 – 21

[14] **A. Cruzado, M. Hartelt, R. Wäsche, M. A. Urchegui, X. Gomez**, *Fretting wear of thin steel wires. Part 1: Influence of contact pressure*, Wear 268 (2010) 1409 – 1416

[15] **Dagang Wang, D. Zhang, S. Ge**, Finite element analysis of fretting fatigue behavior of steel wires and crack initiation, Engineering Failure Analysis, 28 (2013) 47 – 62

[16] **S. Lalonde, R. Guilbault, F. Légeron**, *Modeling multilayered wire strands, a strategy based on 3D finite element beam-to-beam contacts – Part I : Mode formulation and validation*, International Journal of Mechanical Sciences 126 (2017) 281-296

[17] **S. Lalonde, R. Guilbault, F. Légeron**, *Modeling multilayered wire strands, a strategy based on 3D finite element beam-to-beam contacts – Part II : Application to wind-induced vibration and fatigue analysis of overhead conductors*, International Journal of Mechanical Sciences 126 (2017) 281 – 296

[18**] S. Lalonde, R. Guilbault, S. Langlois**, *Numerical analysis of ACSR conductor-clamp systems undergoing wind-induced cyclic loads*, IEEE Transactions on Power Delivery, PP (2017)

[19**] S. Fouvry, P. Kapsa, F. Sidoroff, L. Vincent,** *Identification of the characteristics length scale for fatigue cracking in fretting contacts*, J Phys IV 8 (1998), 159-166

[20] **D. Taylor**, *The theory of critical distances*, Engineering Fracture Mechanics, 75 (2008), 1696-1705

[21] **J.M. Voisin**, **A.B Vannes**, **L. Vincent**, **J. Daviot**, **B. Giraud**, *Analysis of a tube-grid oscillatory contact: methodology for the selection of superficial treatments*, Wear 181–183 (1995) 826–832

[22] **J. A. Araújo, L. Susmel, D. Taylor, J.C.T. Ferro, J.L.A. Ferreira**, *On the prediction of high-cycle fretting fatigue strength: Theory of critical distances vs. hot-spot approach*, Engineering Fracture Mechanics, 75 (2008), 1763-1778

[23] **S. Fouvry, H. Gallien, B. Berthel**, *From uni- to multi-axial fretting-fatigue crack nucleation: Development of a stress-gradient-dependent critical distance approach*, Int. J. Fatigue 62 (2014), 194-209

[24] **C. Gandiolle S. Fouvry**, *Stability of critical distance approach to predict fretting fatigue cracking: a "lopt-bopt" concept*, Int. J. Fatigue 82 (2016), 199-210

[25] **C. Gandiolle, S. Fouvry, E. Charkaluk**, *Lifetime prediction methodology for variable fretting fatigue loading: Plasticity effect*, Int. J. Fatigue 92 (2016), 531-547

[26] **C. Gandiolle, S. Garcin, S. Fouvry**, *A non-collinear fretting-fatigue experiment to compare multiaxial fatigue criteria: critical shear plane strategy is better than invariant formulations*, Tribology International 108 (2017), 57-68

[27] **A. de Pannemaecker, S. Fouvry, J-Y Buffiere**, *Reverse identification of short-long crack threshold fatigue stress intensity factors from plain fretting crack arrest analysis*, Engineering Fracture Mechanics 134 (2015), 267-285

[28] **R. Ferré, S. Fouvry, B. Berthel**, **J-A Ruiz-Sabariego**, *Stress gradient effect on the crack nucleation process of a Ti-6Al-4V titanium alloy under fretting loading : Comparison between non-local fatigue approaches*, Int. J. Fatigue 54 (2013), 55-67

[29] **H. Proudhon, S. Fouvry, J-Y Buffiere**, *A fretting crack initiation prediction taking into account the surface roughness and the crack nucleation process volume*, Int. J. Fatigue 27 (2005), 569-579

[31] **W. Fricke, C. Rawlins**, *Importance of fretting in vibration failures of stranded conductors*, IEEE Transactions on Power Apparatus and Systems, PAS-87 (1968) 1381-1384

[32] **R. B. Kalombo, J. A. Araújo, J.L.A. Ferreira, C.R.M. da Silva, R. Alencar, A. R. Capra,** *Assessment of the fatigue failure of an All Aluminium Alloy Cable (AAAC) for a 230 kV transmission line in the Center-West of Brazil***,** Engineering Failure Analysis 61 (2015), 77-87

[33] **P. Destuynder M. Djaoua**, *Sur une interpretation de l'intégrale de Rice en théorie de la rupture fragile*, Mathematics Methods in the Applied sciences, Vol. 3 (1981), 70-87

[34] **S. Geniaut, P. Massin, N. Moes**, *Evaluation of stress intensiy factors with G-theta method and level sets in CODE_ASTER*, 11th International Conference on Fracture (2005)

[35] **K. Dang Van, M. Maitournam**, *rolling contact in railways: modelling, simulation and damage prediction*, Fatigue and Fracture of Engineering Materials and Structures, Vol 26, Issue 10 (2003), 939-948

[36] **H. Desimone, A. Bernasconi, S. Beretta**, *On the application of Dang Van criterion to rolling contact fatigue*, Wear 260 (2006), 567-572